energies

MDPI

Article

Three-Dimensional Computation Fluid Dynamics Simulation of CO Methanation Reactor with Immersed Tubes

Liyan Sun [1,*], Junjie Lin [2], Dali Kong [2], Kun Luo [2] and Jianren Fan [2]

[1] Institut de Mécanique des Fluides de Toulouse, 31400 Toulouse, France
[2] State Key Laboratory of Clean Energy Utilization, Zhejiang University, Hangzhou 310058, China; linjunjie@zju.edu.cn (J.L.); ywenha@126.com (D.K.); zjuluok@sina.com (K.L.); jrzhjiu@126.com (J.F.)
* Correspondence: liyan.sun@toulouse-inp.fr

Abstract: CO methanation is an exothermic process, and heat removal is an essential issue for the methanation reactor. Numerical studies were carried out to investigate the performance of a 3D fluidized bed methanation reactor with immersed cooling tubes. The simulations were carried out in the frame of the Euler–Euler model to analyze the performance of the reactor. The influences of operating temperatures were studied to understand the reaction characteristics. The temperature increases rapidly neared the inlet due to the reactions. The immersed tubes were effective at removing the reaction heat. The chemical equilibrium state was achieved with an operating temperature of 682 K for the case with immersed tubes. Different control mechanisms can be found during the process of increasing and decreasing the temperature. The reaction kinetic is the dominate factor for the cases with lower temperatures, while the chemical equilibrium will play a more important role at high temperature conditions. The configuration with staggered tubes is beneficial for heat removal.

Keywords: methanation; heat removal; simulation; immersed tubes

Citation: Sun, L.; Lin, J.; Kong, D.; Luo, K.; Fan, J. Three-Dimensional Computation Fluid Dynamics Simulation of CO Methanation Reactor with Immersed Tubes. *Energies* **2022**, *15*, 321. https://doi.org/10.3390/en15010321

Academic Editor: Paweł Ocłoń

Received: 15 November 2021
Accepted: 21 December 2021
Published: 4 January 2022

1. Introduction

Natural gas is an environmentally friendly fuel and has been widely used in civilian applications and industrial fields [1], such as gas turbines, natural gas vehicles, and boilers [2]. In exception for mining from the ground, one possible way is to produce synthetic natural gas (SNG) by methanation. A sustained effort has been made to investigate the methanation technology. The main reactions in the reactor with catalysts are CO methanation and a water–gas shift (WGS) reaction, as follows,

$$CO + 3H_2 \leftrightarrow CH_4 + H_2O \quad \Delta H_{298K} = -206.28\,\mathrm{kJ/mol}$$

$$CO + H_2O \leftrightarrow CO_2 + H_2 \quad \Delta H_{298K} = -41.16\,\mathrm{kJ/mol}$$

The water–gas shift reaction always accompanies the CO methanation when utilizing the Ni catalyst. Also the mixtures of Co, Fe, Ru, Pd, and pt have been proposed and extensively studied for CO methanation [3,4]. Investigations involving the production of SNG by methanation date back to the 1960s. The methanation reactor can be divided into a fixed bed and fluidized bed. Until now, we can find some commercial applications using a fixed bed reactor, such as Lurgi Company, Linde company, and Johnson Matthey [5]. The fluidized bed methanation reactor has some inherent advantages, such as excellent mixing, good heat transfer, and the uniform distribution of temperature [6,7]. The experimental works of the fluidized bed reactor for the methanation process have clearly indicated a superior performance over the fixed bed reactor [8,9]. One of the first fluidized bed methanation reactors for the industry was the Bi-gas-process of bituminous coal research, Inc., which was tested for thousands of hours at a laboratory in 1963 [10]. With the development of computational fluidized dynamics (CFD), numerical simulations become effective tools for investigating the heat and mass transfer in the methanation reactors [11]. The reaction

kinetics were "concluded" by Kopyscinski [8], Li [12], and Chein et al. [13]. Liu et al. [14] simulated the methanation process in the fluidized bed reactor and the products were predicted. The isothermal condition was adopted and the energy conservation equation was not solved in their works. Li et al. [15] carried out the works on the methanation reactor utilizing the structure-based drag model, considering the formation of the cluster. The optimal operating temperature was about 400 degrees. Ngo et al. [16] controlled the temperature of the methanation reactor by feed dilution. Zhang et al. [17] developed a simulation model to predict the hot-spots appearing in the reactor. The distributions of temperature, pressure, and conversion rate were obtained in their work. Li et al. [18] studied the heat removal in a 2D methanation reactor by the two-fluid model. Zhang et al. [19] showed that particle flow and circulation will affect heat removal.

In the literature, relating to the study of the methanation reactor, the authors reached a consensus that temperature is the critical factor for the methanation process. The reaction heat is usually removed from the wall for the lab-scale reactor. However, for the pilot or industrial scale reactor, it is not easy or sufficient to transfer the reaction heat from the center to the wall region [18], which will lead to a fast increase in temperature in the central region. The non-uniform distribution of temperature generates hot-spots, which perhaps leads to the sintering of the catalyst or agglomeration. One feasible scheme is to utilize the immersed tubes in the reactor to withdraw the heat efficiently, but it is rarely reported on in the literature for the three-dimensional methanation reactor and the topic is still open and challenging.

In this work, we focus on the heat removal of the methanation reactor using immersed tubes and the effect of temperature on performance. The two-fluid model is adopted to describe the flow and reaction behavior in the reactor. The reaction characteristics are analyzed under the different operating conditions. The effects of immersed tubes on the conversion of reactants and the selectivity of methane were obtained by simulation (and are discussed). The temperature mechanism on the performance of the methanation reactor is revealed and analyzed. Eventually, this work can provide guidance in the design of the configuration and the optimization of a methanation reactor.

2. Mathematical Models

A Eulerian–Eulerian two-fluid model was adopted to describe the evolution of gas and solid phases. The continuity equation, momentum equation, species transport equation, and energy balance equation were solved in the current work. The kinetic theory of granular flow was adopted for the closure of the model. The governing equations and conservation equations are shown Appendix A. More details can be found in our previous work [20]. The reactions considered in the current work are CO methanation and the water–gas shift reaction. The reaction rates are written as follows [8,13]:

$$R_{METH} = \frac{k_1}{P_{H_2}^{2.5}}\left(P_{CH_4}P_{H_2O} - \frac{P_{H_2}^3 P_{CO}}{K_{eq1}}\right)/DEN^2 \quad (1)$$

$$R_{WGS} = \frac{k_2}{P_{H_2}}\left(P_{CO}P_{H_2O} - \frac{P_{CO_2}P_{H_2}}{K_{eq2}}\right)/DEN^2 \quad (2)$$

$$DEN = 1 + K_{CH_4}P_{CH_4} + K_{CO}P_{CO} + K_{H_2}P_{H_2} + \frac{K_{H_2O}P_{H_2O}}{P_{H_2}} \quad (3)$$

where R_{METH} and R_{WGS} are in the units mol $\cdot$ s$^{-1}\cdot$ kg$_{cat}^{-1}$. The partial pressure of gas species is measured by the unit Pa. R is the ideal gas constant, R = 8.314 J $\cdot$ mol$^{-1}\cdot$ K^{-1}. The constants used in Equations (1)–(3) are calculated based on an Arrhenius-type dependency, and the parameters are listed in Table 1.

The reaction degree of CO methanation and WGS reaction can be evaluated by the conversion rate of reactants and the selectivity of products. Moreover, they can be used for

characterizing the performance of a reactor. The definitions of the conversion rates of CO and H_2 are as follows:

$$X_{CO} = \frac{n_{CO,in} - n_{CO,out}}{n_{CO,in}} \times 100 \quad (4)$$

$$X_{H_2} = \frac{n_{H_2,in} - n_{H_2,out}}{n_{H_2,in}} \times 100 \quad (5)$$

The selectivities of the CH_4 and CO_2 are defined as:

$$S_{CH_4} = \frac{n_{CH_4,out}}{n_{CO,in} - n_{CO,out}} \times 100 \quad (6)$$

$$S_{CO_2} = \frac{n_{CO_2,out}}{n_{CO,in} - n_{CO,out}} \times 100 \quad (7)$$

where n is the molar flow rate of the gaseous components.

Table 1. Kinetic parameters for the calculation of the reaction rate.

Parameter	A	Unit	E	Unit
k_1	3.711×10^{17}	$\text{mol} \cdot \text{s}^{-1}\ \text{kg}_{cat}^{-1}\ \text{Pa}^{-0.5}$	240,100	J/mol
k_2	5.431	$\text{mol} \cdot \text{s}^{-1}\ \text{kg}_{cat}^{-1}\ \text{Pa}^{-0.5}$	67,130	J/mol
$K_{eq,1}$	1.198×10^{23}	Pa^2	26,830	J/mol
$K_{eq,2}$	1.767×10^{-2}		−4400	J/mol
K_{CH_4}	6.65×10^{-9}	Pa^{-1}	−38,280	J/mol
K_{CO}	8.23×10^{-10}	Pa^{-1}	−70,650	J/mol
K_{H_2}	6.12×10^{-14}	Pa^{-1}	−82,900	J/mol
K_{H_2O}	1.77×10^{5}		88,680	J/mol

3. Setup of Simulation

The methanation reactors are shown in Figure 1. The height and width are 0.3 and 0.15 m, respectively. The depth of the reactor is 0.01 m. Reactor (a) is without cooling tubes. Reactor (b), with tubes, is the reference reactor in our work. The amount of cells is 165,300. Reactor (c), with staggered tubes, was used to investigate the influence of the arrangement. The amount of cells for reactor (c) is 165,108. The diameter of the immersed tube is 0.008 m. The horizontal distance between two tubes is 0.012 m. The vertical distance between two rows is 0.016 m. The mixture of CO and H_2 was injected to the reactor from the bottom inlet, with the mole ratio 1:3. The gas inlet rate is 0.35 g/s for the reference case and N_2 was used as the balance gas with 50% mass fraction. The catalyst is the Ni/Al_2O_3 particle with a density of 2000 kg/m^3 and a diameter of 200 µm. The total inventory is 87 g for all cases.

For the simulations, the $k - \varepsilon$ model was adopted to model gas turbulence. The energy conservation equations were solved to obtain the temperature of the gas and solid phase. No-slip boundary conditions for the mean particle velocity was imposed. Outflow conditions were set for the outlet of the reactor with the atmosphere pressure. The code uses a cell-center type finite volume method with a second-order centered scheme in space and a first-order scheme in time. The semi-implicit fractional step method was adopted with iterative linear solvers.

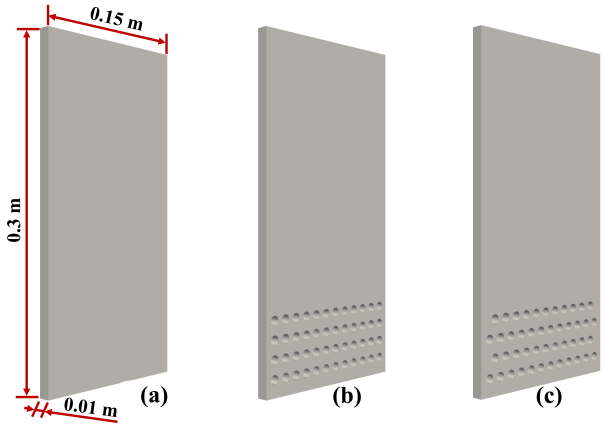

Figure 1. Structure of the fluidized bed methanation reactor. (**a**) without tubes, (**b**) with normal arranged tubes, (**c**) with staggered tubes.

4. Results and Discussion

4.1. Performance of Reactor

The instantaneous distributions of gas components are shown in Figure 2. The nitrogen is used as a balance gas with 50% mass fraction. CO is almost completely converted in the region close to the inlet. H_2 can be found at the outlet, which is the reactant of methanation, but also the product of the water–gas shift reaction. CH_4 is produced simultaneously in the range of 1 centimeter from the inlet. The formation of CO_2 lasts for a longer time and we can find the increase of the mass fraction of CO_2 to the end of bed materials.

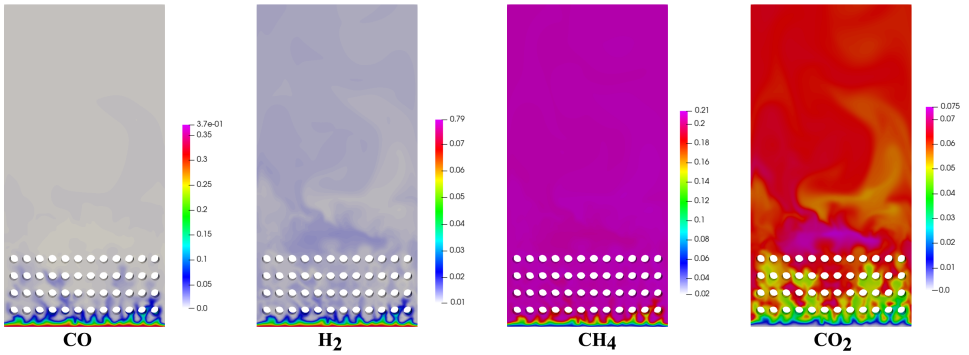

Figure 2. Snapshot of instantaneous mass fraction of gas species. Nitrogen is utilized as balance gas.

The time evolution of gas species mole fraction at the outlet is shown in Figure 3. At the initial time, the reactor is full of nitrogen. After 0.8 s, the products arrive at the outlet of the reactor. The heat removal is 1300 W for the reactor, which is decided after several simulations and theoretical predictions. The mole fraction at the outlet fluctuates around the constant value after 6 s, which illustrates that the system reaches the balance state under current conditions. The main component at the outlet is CH_4 and H_2O. The value of CO is quite low. A certain amount of carbon dioxide is detected at the outlet, which is the product of the water–gas shift reaction. The corresponding conversion rate is shown on the right of Figure 4. The conversion of CO and H_2 are about 0.988 and 0.915, respectively. The lower conversion for H_2 is caused by the production of H_2 by the water–gas shift reaction. The selectivity of CH_4 is 0.902, which indicates that most of the CO has been converted into CH_4. Whilst, the selectivity of CO_2 is about 0.098. Due to the occurrence of the water–gas shift reaction, some reactants are converted into CO_2, which is hard to avoid when utilizing Ni as catalyst.

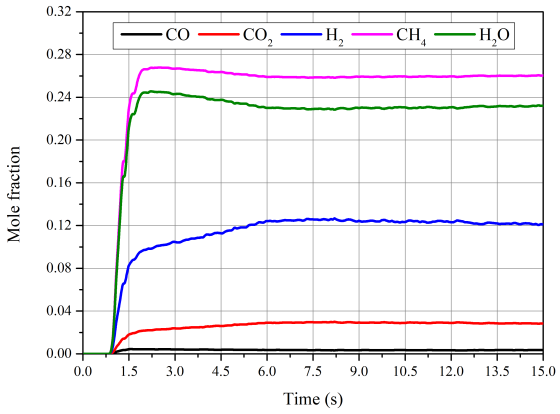

Figure 3. Profile of the time-evolution of the gas species mole fraction at the outlet of the reactor.

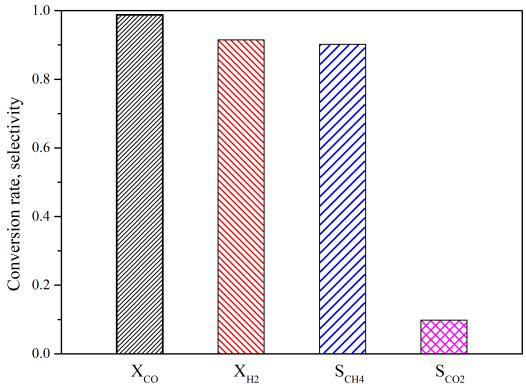

Figure 4. Profile of the time-averaged conversion rate of the reactants and the selectivity of products.

The most concerned and influential parameter in the current work is the temperature, as shown in Figure 5. The highest temperature occurs near the gas inlet. Because the methanation is a strong exothermic reaction, the temperature increases rapidly close to the inlet, with reaction heat released. With the gas and solid moving upward and encountering the tubes, the heat carried by gas and solid phases is removed by the cooling tubes and the temperature decreases. The time-evolution of temperature at the outlet is computed and shown in Figure 6. The temperature increases first and then reaches the nearly constant value after 6 s. Under the current conditions, the final temperature fluctuates around 683 K with heat removal 1300 W.

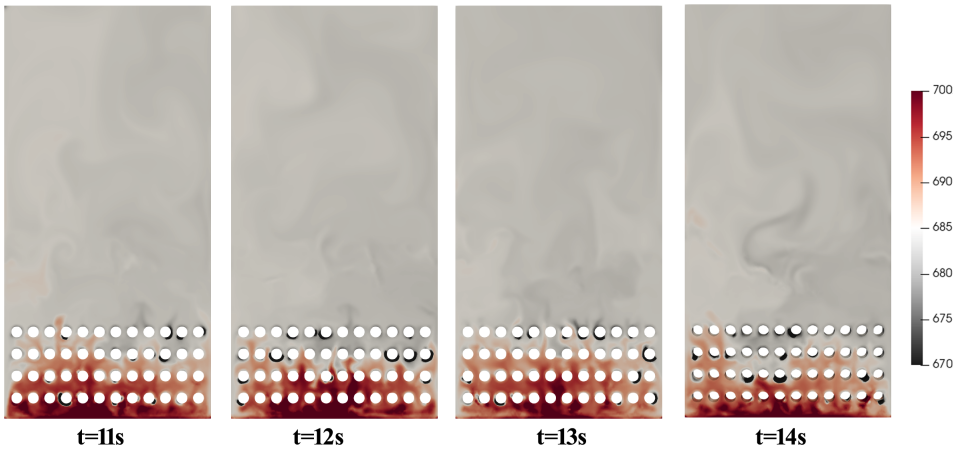

Figure 5. Distribution of instantaneous temperatures at different time points.

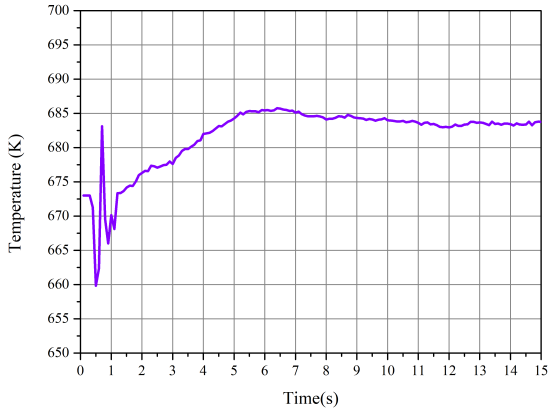

Figure 6. Time-evolution of temperature at the outlet of the methanation reactor.

4.2. Influence of the Temperature

To investigate the influence of temperature on the performance of the methanation process, we carried out the cases with different cooling powers of the immersed tubes, 0 W, 1300 W, and 2000 W, which correspond to the temperature increase process, steady process, and temperature decrease process, to reveal the mechanism of the temperature on the methanation.

The profile of time-evolution gas temperature for different processes is shown in Figure 7. The dashed line represents the reference case with a steady state. With the current gas inlet rate, we found the heat removal of 1300 W was a suitable value for the current condition. For the case without heat removal, the temperature increased linearly to the end of the case. If we set the heat removal at 2000 W, the outlet temperature decreases. For these two dynamic cases, did not have the steady state at the end of the simulations. What we wanted to know was the influence of temperature during the changing process; each case was carried out for 25 s.

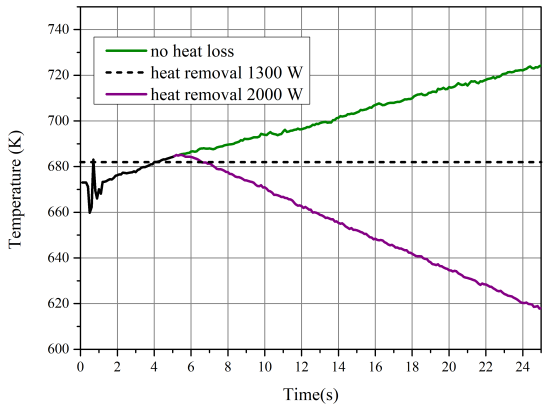

Figure 7. Profile of the time-evolution gas temperature. Dashed line: reference case with heat removal, 1300 W. Green line: no heat removal. Purple line: heat removal 2000 W.

The conversion rates of CO and H_2 are shown in Figure 8. The conversion rates of CO decrease with time for both cases. For the temperature increasing process (black line), the decline is smaller than that for the temperature decreasing process. The conversion rate of H_2 is inversely proportional to the temperature. The same tendency can be found for the selectivity of CH_4, as shown in Figure 9. When increasing the temperature, the selectivity of CO_2 increases. It means that more reactants are converted into CO_2 and we get less CH_4 when we raise the operating temperature from steady state. Considering both the Figures 8 and 9, we get that during the process of increasing the temperature, the water–gas shift reaction and reverse reaction were enhanced. The original chemical equilibrium was interrupted. By decreasing the temperature, more CH_4 are generated and we get less

CO_2. The conversion of CO decreases due to the decreases of reaction kinetics. Until now, we know when the temperature is higher than the critical stability value, the chemical equilibrium is the dominant factor; when the temperature is lower than the critical stability value, the reaction is limited by the kinetics.

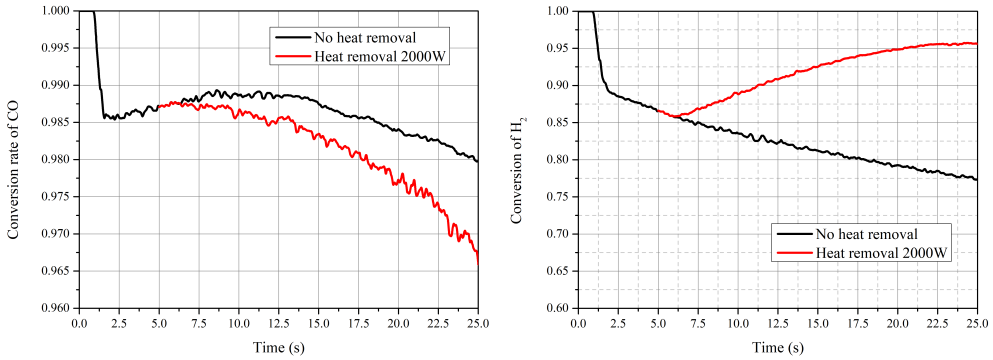

Figure 8. Time-evolution of conversion rate of CO (**left**) and H_2 (**right**).

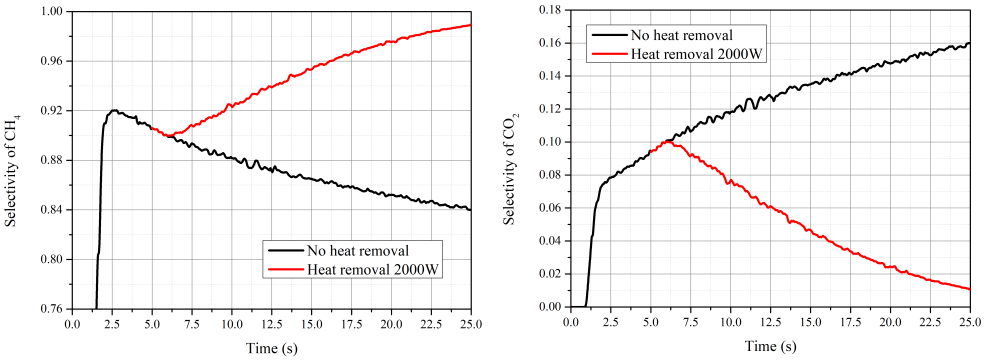

Figure 9. Time-evolution of selectivity of CH_4 (**left**) and CO_2 (**right**).

4.3. Influence of Flow Behavior

To investigate the influence of dynamic behavior, we tested the cases with different inlet rates. The flow rate of CO and H_2 kept constant for all of the simulations to produce the same amount of reaction heat. The balance gas, N_2, was adjusted to generate the different flow patterns and the flow rates of N_2 are 0.070 g/s, 0.175 g/s and 0.345 g/s, respectively. The solid volume fraction is shown in Figure 10. The bed expanded height increases with the inlet rate. More (and larger) bubbles are formed around the tubes for the case with the higher gas inlet rate. The corresponding conversion rate of reactants and selectivity of products are shown in Figure 11. The CO conversion decreases with the inlet rate under the combining effect of residence time and the heat transfer. The conversion of H_2 and selectivity of CH_4 increase with the inlet rate. The selectivity of CO_2 decreases with inlet rate.

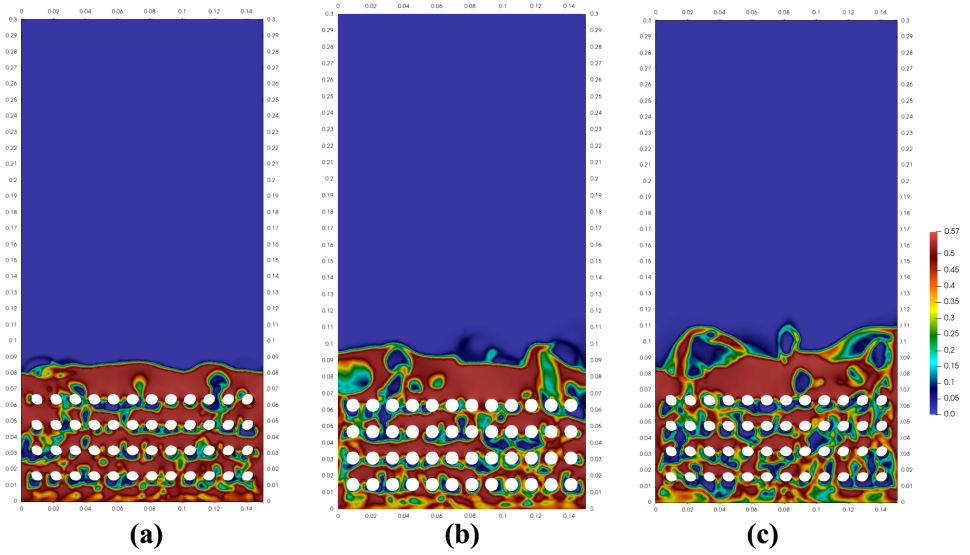

Figure 10. Profile of the solid volume fraction with different fluidization gas inlet rate; (**a**) 0.245 g/s, (**b**) 0.35 g/s, (**c**) 0.525 g/s.

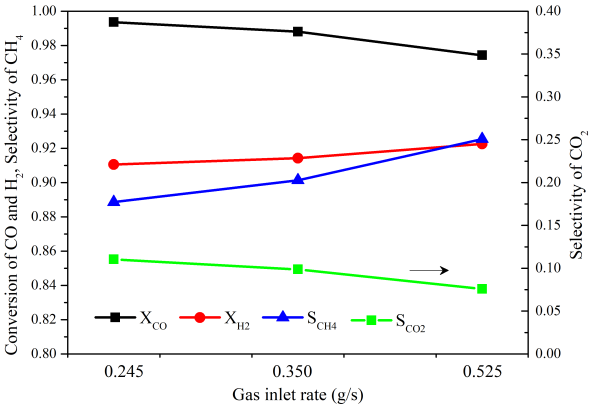

Figure 11. Conversion rate of reactants and selectivity of products with different fluidization gas rates.

4.4. Influence of the Arrangement of Tubes

Three arrangements of immersed tubes are discussed in this section. The basic one is without tubes. The normal arrangement of tubes has been discussed in the first part of this section. The performance of the staggered tubes are shown in Figure 12. Compared with Figure 5, the temperature in the reactor with staggered tubes is lower than the reference case, which indicates the heat removal efficiency is higher with staggered tubes and the region with high temperature becomes narrow. The second sub-figure in Figure 12 shows the flow pattern with staggered tubes. CO_2 is generated in the whole bed. We can find that methane is produced between the first and second row of tubes at the last sub-figure.

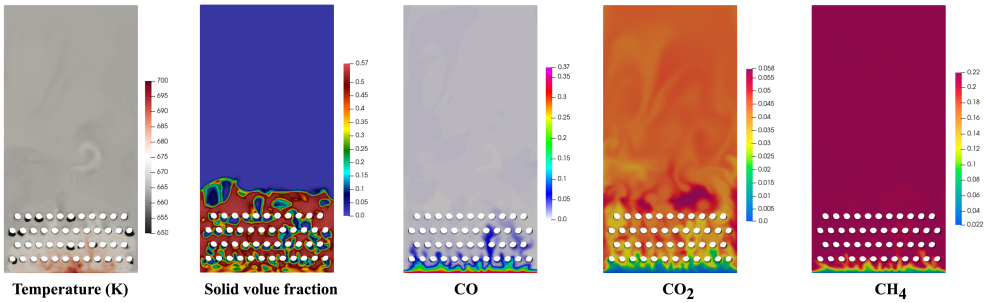

Figure 12. Instantaneous distribution of temperature, solid volume fraction, mass fraction of CO, CO_2, and CH_4.

The Nusselt number is computed and shown in Figure 13. The highest value of Nu for the staggered tubes case is larger than the reference case, which illustrates a larger heat transfer between the fluid and tubes. The gas velocity is shown on the right of Figure 13. For the case with staggered tubes, the gas detours between different rows of tubes. However, for the reference case, most gas will traverse the bed material without passing the channel between the rows. This leads to a lower performance of heat transfer for the reference case.

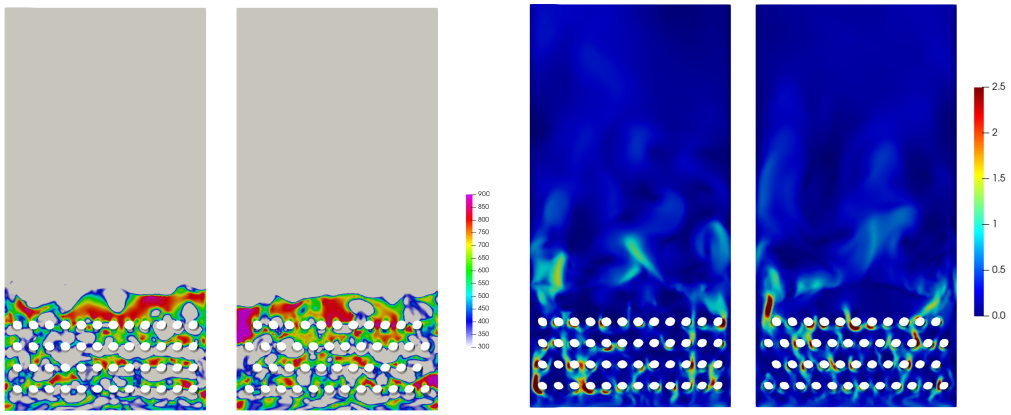

Figure 13. (**Left**): instantaneous distribution of the Nusselt number. (**Right**): instantaneous distribution of gas velocity.

The conversion rate of reactants and selectivity of products for different plans of the reactors are shown in Figure 14 for quantitative analysis. The conversion rate of CO is quite high for all three cases. The case without tubes produces the least amount of CH_4 and the largest of CO_2 due to the reaction heat is not removed from the center of the reactor. Comparisons between the reference case and staggered arrangements of tubes show that the production of CH_4 is larger with staggered tubes, and the lowest selectivity of CO_2 was observed. The results indicate the optimal configuration should be the staggered one, which corresponds to the most effective removal of the reaction heat.

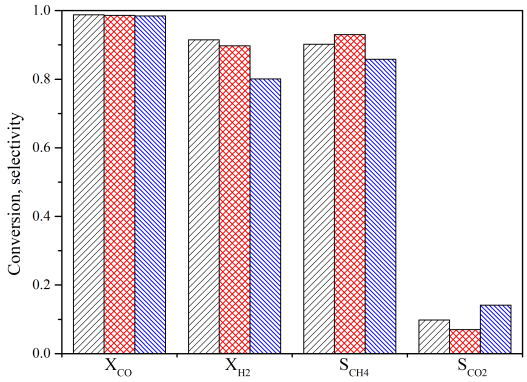

Figure 14. Conversion rate and selectivity under different configuration. Black column: normal arrangement of tubes. Red column: staggered arrangement of tubes. Blue column: without tubes.

The interaction coefficient between phases are shown in Figure 15. The drag coefficient decreases with solid volume fraction. With the high solid volume fraction, the interaction between gas and solid is nearly the same for the case with normal arrangement and staggered arrangement. Difference between two configurations can be found at low solid volume fraction as shown on the right of Figure 15, the staggered tubes lead to a lower drag coefficient. The difference of the micro-dynamic behavior will finally generate the different performances of the reactor.

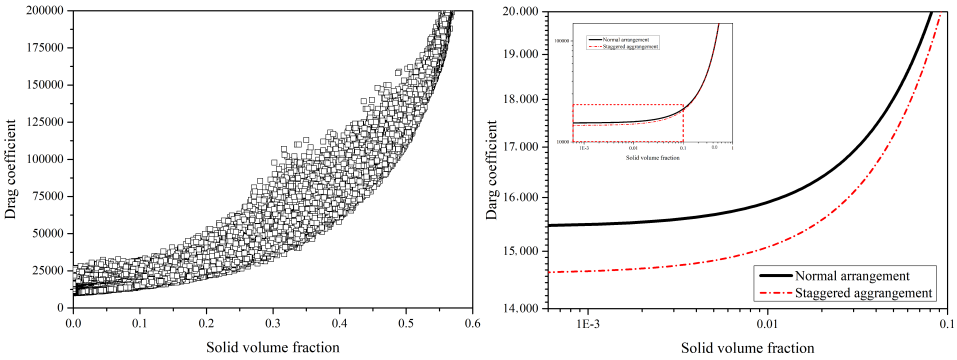

Figure 15. (**Left**): distribution of the drag coefficients for the case with staggered tubes. (**Right**): fitting results of the drag coefficient for different arrangement of tubes.

5. Conclusions

This numerical study was carried out to better understand the CO methanation process in a three-dimensional fluidized bed reactor utilizing a Euler–Euler two-fluid model. The performance of the methanation reactor and reaction characteristics were obtained and analyzed. The reaction heat removal was realized by the immersed tubes in the reactor. The influences of operating parameters on the production of methane were studied. Based on the current results, some essential issues can be explained, and the following conclusions can be drawn:

- The chemical equilibrium of the methanation process was achieved during the CFD simulation with effective heat removal by immersed pipes, and the preferable temperature was about 682 K. The results also show that the temperature has an essential impact on the production of methane.
- The reaction finished near the inlet of the reactor, and then the main process was the mixing of the gas components. The CO vanished for each operating condition and the conversion rate was higher than 98%. The highest value of selectivity of methane was 92 % under current operating conditions.
- During the process of increasing temperature from the steady condition, the water–gas shift reaction and reverse reactions played a more important role for the performance of

the reactor. The production rate of CH_4 decreased and more reactants were converted into CO_2. Chemical equilibrium was the decisive factor during the process with increasing temperature.

- With the decrease in temperature, the effect of the reaction kinetic became the dominant factor. The selectivity of CH_4 increased, whilst the conversion rate of CO decreased due to the low reaction rate.
- The arrangement of the tubes will influence the interaction between the fluid and tubes. The staggered tubes are beneficial for the effective removal of reaction heat. The selectivity of methane with staggered tubes was 3% higher than that with normal tubes.
- The effect of the structures of the tubes, including the diameter, distance between tubes, and the amount of tubes, should be studied to determine the construction at the next stage.

Author Contributions: Conceptualization, J.L., L.S. and K.L.; methodology, D.K., L.S. and K.L.; software, L.S., K.L. and J.F.; validation, L.S., K.L. and J.F.; writing—review and editing, L.S., J.L., D.K., L.S., K.L. and J.F.; supervision, J.F. All authors have read and agreed to the published version of the manuscript.

Funding: This research was funded by the National Natural Science Foundation of China (nos. 51806192, 51925603) and the National Key Research and Development Plan (no. 2017YFE0112500).

Informed Consent Statement: Not applicable.

Data Availability Statement: Data available in a publicly accessible repository.

Conflicts of Interest: The authors declare no conflict of interest.

Appendix A. Governing Equations

A two-fluid model in the frame of the Eulerian–Eulerian model coupling with kinetic theory of granular flow was adopted in this work. Both gas phase and solid phase are regarded as a continuum medium. The continuity equations for gas phase and solid phase are written as follows,

$$\frac{\partial(\alpha_g \rho_g)}{\partial t} + \bigtriangledown \cdot (\alpha_g \rho_g \mathbf{u}_g) = 0 \tag{A1}$$

$$\frac{\partial(\alpha_s \rho_s)}{\partial t} + \bigtriangledown \cdot (\alpha_s \rho_s \mathbf{u}_s) = 0 \tag{A2}$$

where α, ρ and $\mathbf{u}$ represent volume fraction, density, and velocity, respectively. Only homogeneous reactions are taken into consideration and the source term for mass transfer between phases is zero.

The momentum equations are

$$\frac{\partial \alpha_g \rho_g \mathbf{u}_g}{\partial t} + \bigtriangledown \cdot (\alpha_g \rho_g \mathbf{u}_g \mathbf{u}_g) = -\alpha_g \bigtriangledown p + \bigtriangledown \cdot (\tau_g) + \alpha_g \rho_g \mathbf{g} + \beta(\mathbf{u}_s - \mathbf{u}_g) \tag{A3}$$

$$\frac{\partial \alpha_s \rho_s \mathbf{u}_s}{\partial t} + \bigtriangledown \cdot (\alpha_s \rho_s \mathbf{u}_s \mathbf{u}_s) = -\alpha_s \bigtriangledown p - \bigtriangledown p_s + \bigtriangledown \cdot (\tau_s) + \alpha_s \rho_s \mathbf{g} + \beta(\mathbf{u}_g - \mathbf{u}_s) \tag{A4}$$

where τ_g and τ_s are the stress tensors for the gas and solid phase,

$$\tau_g = \mu_g[\bigtriangledown \mathbf{u}_g + (\bigtriangledown \mathbf{u}_g)^T] - \frac{2}{3}\mu_g(\bigtriangledown \cdot \mathbf{u}_g)I \tag{A5}$$

$$\tau_s = \mu_s[\bigtriangledown \mathbf{u}_s + (\bigtriangledown \mathbf{u}_s)^T] - (\lambda_s - \frac{2}{3}\mu_s)(\bigtriangledown \cdot \mathbf{u}_s)I \tag{A6}$$

μ represents the shear viscosity,

$$\mu_s = \frac{4}{5}\alpha_s^2 \rho_s d_s g_0 (1+e)\sqrt{\frac{\theta}{\pi}} + \frac{10\rho_s d_s \sqrt{\pi\theta}}{96(1+e)\alpha_s g_0}\left[1 + \frac{4}{5}g_0 \alpha_s (1+e)\right]^2 \tag{A7}$$

$$\mu_g = C_\mu \frac{k^2}{\varepsilon} \tag{A8}$$

The solid pressure is calculated based on kinetic theory of granular flow, as follows,

$$p_s = \alpha_s \rho_s \theta + 2\rho_s(1+e)\alpha_s^2 g_0 \theta \tag{A9}$$

and g_0 is the radial distribution function,

$$g_0 = \left[1 - \left(\frac{\alpha_s}{\alpha_{s,max}}\right)^{1/3}\right]^{-1} \tag{A10}$$

The momentum transfer coefficient between phases is,

$$\beta = \begin{cases} \frac{3}{4}\left(\frac{C_D \alpha_g \alpha_s \rho_g |\mathbf{u}_g - \mathbf{u}_s|}{d_s}\right)\alpha_s^{-2.65} & \alpha_s < 0.2 \\ 150\left(\frac{\mu_g \alpha_s^2}{\alpha_s d_s^2}\right) + 1.75\left(\frac{\alpha_s \rho_g}{d_s}\right)|\mathbf{u}_g - \mathbf{u}_s| & \alpha_s \geq 0.2 \end{cases} \tag{A11}$$

$$C_D = \begin{cases} \frac{24}{R_e \alpha_g}\left[1 + 0.15(R_e \alpha_g)^{0.687}\right] & R_e < 1000 \\ 0.44 & R_e \geq 1000 \end{cases} \tag{A12}$$

where the Reynolds number is written as

$$R_e = \frac{\rho_g d_s |\mathbf{u}_g - \mathbf{u}_s|}{\mu_g} \tag{A13}$$

The kinetic theory of granular flow is adopted in the current work for the closure of the model. The transport equation of granular temperature is

$$\frac{3}{2}\left[\frac{\partial}{\partial t}(\alpha_s \rho_s \theta) + \bigtriangledown \cdot (\alpha_s \rho_s \theta)\mathbf{u}_s\right] = (-\bigtriangledown p_s \mathbf{I} + \tau_s) : \bigtriangledown u_s + \bigtriangledown \cdot (k_s \bigtriangledown \theta) - \gamma_s - 3\beta\theta + D_{gs} \tag{A14}$$

where D_{gs} and γ_s are written as,

$$D_{gs} = \frac{d_s \rho_s}{4\sqrt{\pi\theta} g_0}\left(\frac{18\mu_g}{d_s^2 \rho_s}\right)^2 |u_g - u_s|^2 \tag{A15}$$

$$\gamma_s = \frac{1}{3}(1-e^2)\frac{\frac{3}{2}\theta}{\tau_s^c} \tag{A16}$$

k_s represents the conductivity of fluctuating energy,

$$k_s = \frac{25\rho_s d_s \sqrt{\pi\theta}}{64(1+e)g_0}\left[1 + \frac{6}{5}(1+e)g_s \alpha_s\right]^2 + 2\alpha_s^2 \rho_s d_s g_0 (1+e)(\frac{\theta}{\pi})^{1/2} \tag{A17}$$

$k - \varepsilon$ is adopted in our work for the closure of the model,

$$\frac{\partial}{\partial t}(\alpha_g \rho_g k) + \bigtriangledown \cdot (\alpha_g \rho_g u_g k) = \bigtriangledown \cdot \left(\alpha_g \frac{\mu_t}{\sigma_k} \bigtriangledown k\right) + \alpha_g G_k - \alpha_g \rho_g \varepsilon \tag{A18}$$

$$\frac{\partial}{\partial t}(\alpha_g \rho_g \varepsilon) + \bigtriangledown \cdot (\alpha_g \rho_g u_g \varepsilon) = \bigtriangledown \cdot \left(\alpha_g \frac{\mu_t}{\sigma_\varepsilon} \bigtriangledown \varepsilon\right) + \alpha_g \frac{\varepsilon}{k}(C_1 G_K - C_2 \rho_g \varepsilon) - \alpha_g \rho_g \varepsilon \tag{A19}$$

where G_k is the generation of turbulence kinetic energy,

$$G_k = \mu_t \bigtriangledown u_g \cdot [\bigtriangledown u_g + \bigtriangledown u_g^T] - \frac{2}{3} \bigtriangledown u_g (\mu_t \bigtriangledown u_g + \rho_g k) \tag{A20}$$

The transport equations of energy for the gas phase and solid phase are

$$\frac{\partial}{\partial t}(\alpha_g \rho_g H_g) + \bigtriangledown \cdot (\alpha_g \rho_g \mathbf{u}_g H_g) = \bigtriangledown (\kappa_g \bigtriangledown T_g) + h(T_g - T_s) + S_g \tag{A21}$$

$$\frac{\partial}{\partial t}(\alpha_s \rho_s H_s) + \bigtriangledown \cdot (\alpha_s \rho_s \mathbf{u}_s H_s) = \bigtriangledown (\kappa_s \bigtriangledown T_s) + h(T_s - T_g) + S_s \tag{A22}$$

where h is the heat transfer coefficient,

$$h = \frac{6\alpha_s \alpha_g \lambda_g Nu}{d_p^2} \tag{A23}$$

$$Nu = (7 - 10\alpha_g + 5\alpha_g^2)(1 + 0.7Re^{0.2}Pr^{1/3}) + (1.33 - 2.4\alpha_g + 1.2\alpha_g^2)Re^{0.7}Pr^{1/3} \tag{A24}$$

and the Prandtl number is calculated as,

$$Pr = \frac{\mu_g C_g}{\lambda_g} \tag{A25}$$

The transport equation for the gas species is

$$\frac{\partial \alpha_g \rho_g Y_{g,i}}{\partial t} + \bigtriangledown \cdot (\alpha_g \rho_g \mathbf{u}_g Y_{g,i}) = \bigtriangledown \cdot (\alpha_g J_{g,i}) + \psi_{g,i} \tag{A26}$$

where $\psi_{g,i}$ is the source term due to reactions. The species for solid particles keep constant.

References

1. Kopyscinski, J.; Schildhauer, T.J.; Biollaz, S.M.A. Employing Catalyst Fluidization to Enable Carbon Management in the Synthetic Natural Gas Production from Biomass. *Chem. Eng. Technol.* **2009**, *32*, 343–347. [CrossRef]
2. Hussain, I.; Jalil, A.; Hassan, N.; Farooq, M.; Mujtaba, M.; Hamid, M.; Sharif, H.; Nabgan, W.; Aziz, M.; Owgi, A. Contemporary thrust and emerging prospects of catalytic systems for substitute natural gas production by CO methanation. *Fuel* **2021**, 122604. [CrossRef]
3. Gao, J.; Liu, Q.; Gu, F.; Liu, B.; Zhong, Z.; Su, F. Recent advances in methanation catalysts for the production of synthetic natural gas. *RSC Adv.* **2015**, *5*, 22759–22776. [CrossRef]
4. Liu, P.; Zhao, B.; Li, S.; Shi, H.; Ma, M.; Lu, J.; Yang, F.; Deng, X.; Jia, X.; Ma, X.; et al. Influence of the Microstructure of Ni–Co Bimetallic Catalyst on CO Methanation. *Ind. Eng. Chem. Res.* **2020**, *59*, 1845–1854. [CrossRef]
5. Rönsch, S.; Schneider, J.; Matthischke, S.; Schlüter, M.; Götz, M.; Lefebvre, J.; Prabhakaran, P.; Bajohr, S. Review on methanation – From fundamentals to current projects. *Fuel* **2016**, *166*, 276–296. [CrossRef]
6. Kopyscinski, J.; Schildhauer, T.J.; Biollaz, S.M. Methanation in a fluidized bed reactor with high initial CO partial pressure: Part II— Modeling and sensitivity study. *Chem. Eng. Sci.* **2011**, *66*, 1612–1621. [CrossRef]
7. Eri, Q.; Peng, J.; Zhao, X. CFD simulation of biomass steam gasification in a fluidized bed based on a multi-composition multi-step kinetic model. *Appl. Therm. Eng.* **2018**, *129*, 1358–1368. [CrossRef]
8. Kopyscinski, J.; Schildhauer, T.J.; Biollaz, S.M. Methanation in a fluidized bed reactor with high initial CO partial pressure: Part I—Experimental investigation of hydrodynamics, mass transfer effects, and carbon deposition. *Chem. Eng. Sci.* **2011**, *66*, 924–934. [CrossRef]
9. Kopyscinski, J.; Schildhauer, T.J.; Biollaz, S.M.A. Fluidized-Bed Methanation: Interaction between Kinetics and Mass Transfer. *Ind. Eng. Chem. Res.* **2011**, *50*, 2781–2790. [CrossRef]
10. Cobb, J.T.; Streeter, R.C. Evaluation of Fluidized-Bed Methanation Catalysts and Reactor Modeling. *Ind. Eng. Chem. Process Des. Dev.* **1979**, *18*, 672–679. [CrossRef]
11. Yu, H.; Zhang, H.; Buahom, P.; Liu, J.; Xia, X.; Park, C.B. Prediction of thermal conductivity of micro/nano porous dielectric materials: Theoretical model and impact factors. *Energy* **2021**, *233*, 121140. [CrossRef]
12. Li, J.; Yang, B. Multi-scale CFD simulations of bubbling fluidized bed methanation process. *Chem. Eng. J.* **2019**, *377*, 119818. [CrossRef]
13. Chein, R.Y.; Yu, C.T.; Wang, C.C. Numerical simulation on the effect of operating conditions and syngas compositions for synthetic natural gas production via methanation reaction. *Fuel* **2016**, *185*, 394–409. [CrossRef]
14. Liu, Y.; Hinrichsen, O. CFD Simulation of Hydrodynamics and Methanation Reactions in a Fluidized-Bed Reactor for the Production of Synthetic Natural Gas. *Ind. Eng. Chem. Res.* **2014**, *53*, 9348–9356. [CrossRef]
15. Li, J.; Yang, B. Bubbling fluidized bed methanation study with resolving the mesoscale structure effects. *AIChE J.* **2019**, *65*, 16561. [CrossRef]

16. Ich Ngo, S.; Lim, Y.I.; Lee, D.; Won Seo, M.; Kim, S. Experiment and numerical analysis of catalytic CO_2 methanation in bubbling fluidized bed reactor. *Energy Convers. Manag.* **2021**, *233*, 113863. [CrossRef]
17. Zhang, W.; Machida, H.; Takano, H.; Izumiya, K.; Norinaga, K. Computational fluid dynamics simulation of CO_2 methanation in a shell-and-tube reactor with multi-region conjugate heat transfer. *Chem. Eng. Sci.* **2020**, *211*, 115276–115285. [CrossRef]
18. Li, J.; Agarwal, R.K.; Yang, B. Two-Dimensional Computational Fluid Dynamics Simulation of Heat Removal in Fluidized Bed Methanation Reactors from Coke Oven Gas Using Immersed Horizontal Tubes. *Ind. Eng. Chem. Res.* **2020**, *59*, 981–991. [CrossRef]
19. Zhang, Q.; Cao, Z.; Ye, S.; Sha, Y.; Chen, B.; Zhou, H. Mathematical modeling for bubbling fluidized bed CO-methanation reactor incorporating the effect of circulation and particle flows. *Chem. Eng. Sci.* **2022**, *249*, 117305. [CrossRef]
20. Sun, L.; Luo, K.; Fan, J. 3D Unsteady Simulation of a Scale-Up Methanation Reactor with Interconnected Cooling Unit. *Energies* **2021**, *14*, 7095. [CrossRef]